scientific reports

Check for updates

OPEN

Improved conversion of carbon dioxide to methane via photohydrogenation using Gd_2NiMnO_6 with a dendritic fibrous architecture

Ping Yan[1], Dulong Feng[2], Qian Wan[5], Shulong Liu[3,4,5] & Seyed Mohsen Sadeghzadeh[6]✉

The conversion of diluted CO_2 into high-energy fuels is increasingly central to renewable energy research. This study investigates the efficacy of a Gd_2NiMnO_6 dendritic nanofibrous (DNF) photocatalyst in transforming carbon dioxide to methane through photoreduction. Gd_2NiMnO_6 DNF was found to provide active adsorption sites and control the strand dimensions for metal groups, facilitating the chemical absorption of CO_2. The light-driven photoreduction of CO_2 to CH_4 through biomass valorization has become a sustainable focus area, with photocatalytic CO_2 reduction recognized as a key strategy to mitigate greenhouse gases and achieve carbon neutrality. However, designing active sites with enhanced selectivity and efficiency for CO_2 photoreduction remains challenging. Reducing carbon dioxide is especially crucial in the era of petroleum refineries. This work introduces a reusable, magnetically responsive nanocatalyst for the targeted light reduction of CO_2 to CH_4, utilizing eco-friendly methods, mild thermal conditions, ambient pressure, and sustainable dehydrating agents. This approach provides significant economic benefits and compatibility with functional groups, highlighting the potential of combining 3D nanoparticle structures with sustainable chemistry to create highly efficient catalytic systems for CO_2 to CH_4 conversion.

Keywords Nanocatalyst, Green chemistry, Gd_2NiMnO_6, Nanoceramic, Dendritic nanofibrous, UV-Vis irradiation

Abbreviations

DNF	Dendritic Nanofibrous
CO_2	Carbon dioxide
CH_4	Methane
XRD	X-ray diffraction
TEM	Transmission electron microscopy
SEM	Scanning electron microscope
EDX	Energy-dispersive X-ray
BET	Brunauer-Emmett-Teller
TPC	Transient photocurrent
PL	Photoluminescence
EIS	Electrochemical impedance spectroscopy

Global energy demands and the pressing issue of climate change have driven significant interest in the sustainable conversion of CO_2 into valuable carbon-based products like CO and hydrocarbon fuels[1]. Photocatalytic CO_2

[1]School of Life Sciences, Huaibei Normal University, Huaibei 235000, China. [2]Anhui Guangbo Mechanical Electronic Manufacturing Co., Ltd, Huaibei 235000, China. [3]Anhui Province Industrial Generic Technology Research Center for Alumics Materials, Huaibei Normal University, Huaibei 235000, China. [4]Anhui Province Key Laboratory of Intelligent Computing and Applications, Huaibei Normal University, Huaibei 235000, China. [5]School of Physics and Electronic Information, Huaibei Normal University, Huaibei 235000, China. [6]New materials Technology and Processing Reserearch Center, Neyshabur Branch, Islamic Azad University, Neyshabur, Iran. ✉email: Seyedmohsen.sadeghzadeh@gmail.com; M.sadeghzadeh@iau-neyshabur.ac.ir

reduction is a crucial pathway for converting solar energy into chemical energy, inspired by the natural process of photosynthesis. Considerable efforts have been made to develop photocatalysts capable of capturing and reducing CO_2 effectively[2]. However, the efficiency of existing photocatalysts remains inadequate due to challenges such as limited surface area, restricted active sites, and rapid recombination of photogenerated electron–hole pairs[3]. Photocatalysts, when exposed to light, generate electron–hole pairs that must separate and transfer to specific sites to facilitate redox reactions. The efficiency of charge separation and the directed movement of excitons are critical factors influencing catalytic performance[4]. Enhancing the CO_2 adsorption capacity of photocatalysts is a promising approach to boost CO_2 conversion efficiency, as stable and effective binding interactions with CO_2 molecules are essential for efficient electron transfer from active catalytic sites[5].

Gd_2NiMnO_6, a member of the bismuth-based semiconductor family, has shown promising potential in photocatalysts and gas sensors due to its unique pyrochlore architecture and suitable energy band of 2.6–2.9 eV[6]. The Gd_2NiMnO_6 octahedron structure, which consists of a six O and single Mn, is interconnected by shared vertices[7–9]. This interconnected vertex arrangement enhances the conveyance and segregation of photo-induced carriers, making Gd_2NiMnO_6 a promising material for efficient visible-light photocatalysis[10,11]. Since the photocatalytic reaction primarily takes place on the surface, the photocatalyst's surface and morphology microstructure significantly influence the photocatalytic kinetics, making the surface morphology control of Gd_2NiMnO_6 a research focus.

In recent years, there has been a strong emphasis on sustainable and eco-friendly development, particularly in aligning energy and environmental needs[12]. Various approaches have been thoroughly explored, including emission reduction, chemical degradation, pollutant removal, and energy conservation[13–16]. Converting carbon dioxide to methane has emerged as a strategy that not only aids energy conservation but also helps to mitigate greenhouse gas effects both crucial for addressing energy shortages and environmental pollution[17–20]. Consequently, finding the optimal photocatalyst has become a significant focus, with prior studies examining materials like ZnO, SnO_2, and CeO_2[21–28]. The demand for new, resilient photocatalysts that are highly active, cost-effective, and easy to synthesize for gas-phase reduction of low-concentration CO_2 with water vapor remains high[29–31]. Efficient photocatalysts capable of directly using low-concentration CO_2 from gas sources offer practical advantages such as energy and cost savings, as well as simplified processing[32–36].

This research presents the first reported fabrication of Gd_2NiMnO_6 dendritic nanofiber (DNF) photocatalysts using a simple hydrothermal synthesis combined with stir-assisted techniques. These samples were engineered specifically to target CO_2 as a primary pollutant, with their adsorption and photocatalytic activity under visible light thoroughly evaluated. Advanced characterization methods, including XRD, TEM, and UV-Vis, were used to analyze the microscopic structure and photocatalytic properties of the synthesized samples. The study aims to develop Gd_2NiMnO_6 DNF for the photoreduction of CO_2 to CH_4, induced by UV light, offering an innovative and eco-friendly approach that exhibits high efficiency and selectivity. UV-Vis irradiation was applied to reduce CO_2 levels and mitigate H_2 stress, aligning the process with European environmental standards.

Experimental

Synthesis of Gd2NiMnO6 DNF

The Gd_2NiMnO_6 DNF was synthesized via a microwave radiation technique. In this process, a solution containing 0.8 mmol of $Mn(NO_3)_2{\cdot}4\ H_2O$, 1.2 mmol of $Gd(NO_3)_3$, and 1.2 mmol of $Ni(NO_3)_2$ was prepared in 40 ml of 1-pentanol and 180 ml of cyclohexane solution and thoroughly stirred. Ascorbic acid (2 ml, 0.05 M) and cetylpyridinium bromide (1.2 g) were then added to maintain a pH level of 10. The resulting precipitates were separated by centrifugation, washed multiple times with methanol, and subsequently dried at 165 °C.

Catalytic hydrogenation of CO2

In this procedure, a stainless-steel reactor with a 100 mL capacity and high-pressure capabilities was loaded with 8 mg of catalyst and 10 mL of a 2 M potassium hydroxide solution. Prior to initiating the reaction, nitrogen gas was used to purge the vessel, ensuring the removal of any residual air. A 1:1 mixture of carbon dioxide and hydrogen gas was introduced into the reactor at room temperature, with stirring maintained at 250 rpm. After a reaction time of 30 min, the heating mantle was removed, and the reactor was allowed to cool gradually to room temperature. Once cooled, the pressure in the reactor was lowered, and the reaction mixture was transferred to a sample container. This mixture was then centrifuged to separate the Gd_2NiMnO_6 DNF.

Results and discussion

The Gd_2NiMnO_6 DNF compound was synthesized using an efficient bifurcated approach, designed to integrate Gd_2NiMnO_6 DNF as a supportive component within the nanofiber structure. In this configuration, Gd_2NiMnO_6 DNF acted as focal sites for catalytic enhancement on its external surface. To understand the mechanisms involved, SEM and TEM analyses were conducted on the cells. As illustrated in Fig. 1, the Gd_2NiMnO_6 DNF appeared as three-dimensional dendritic fibers, forming structural walls that increased the available surface area.

X-ray diffraction (XRD) analysis was performed to examine the crystalline structure of the Gd_2NiMnO_6 DNF composite photocatalyst. In Fig. 2, distinctive peaks at $2\theta = 57.02°$, 48.13°, 33.56°, and 28.92° are observed, corresponding to the (622), (440), (400), and (222) planes of Gd_2NiMnO_6 DNF, in alignment with JCPDS No.87–0284. These results confirm the successful synthesis of the composite photocatalyst. The EDS spectrum in Fig. 3 illustrates the elemental composition and chemical analysis, revealing the presence of Gd, Ni, Mn, and O in the Gd_2NiMnO_6 DNF. The XPS spectrum shown in Fig. 4 provides an overview of the elemental composition and chemical makeup. The comprehensive survey of Gd_2NiMnO_6 DNF confirms the presence of Gd, Ni, Mn, and O elements.

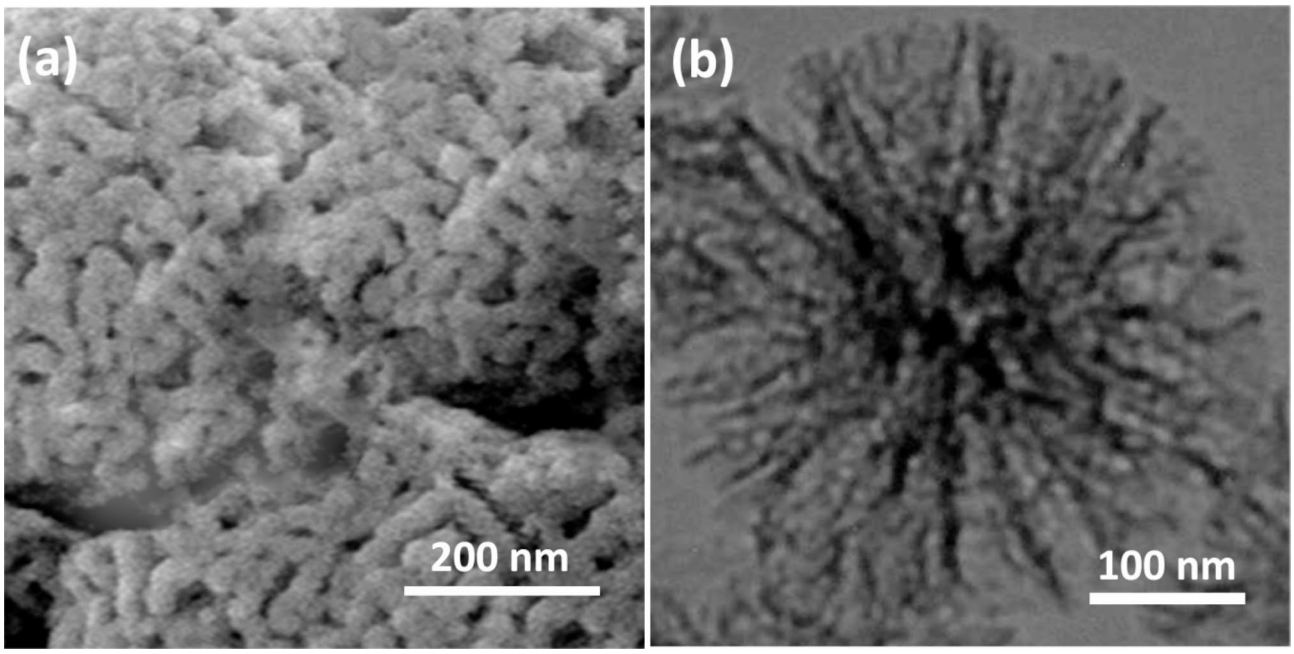

Fig. 1. FESEM images of Gd_2NiMnO_6 DNF (**a**); and TEM of Gd_2NiMnO_6 DNF (**b**).

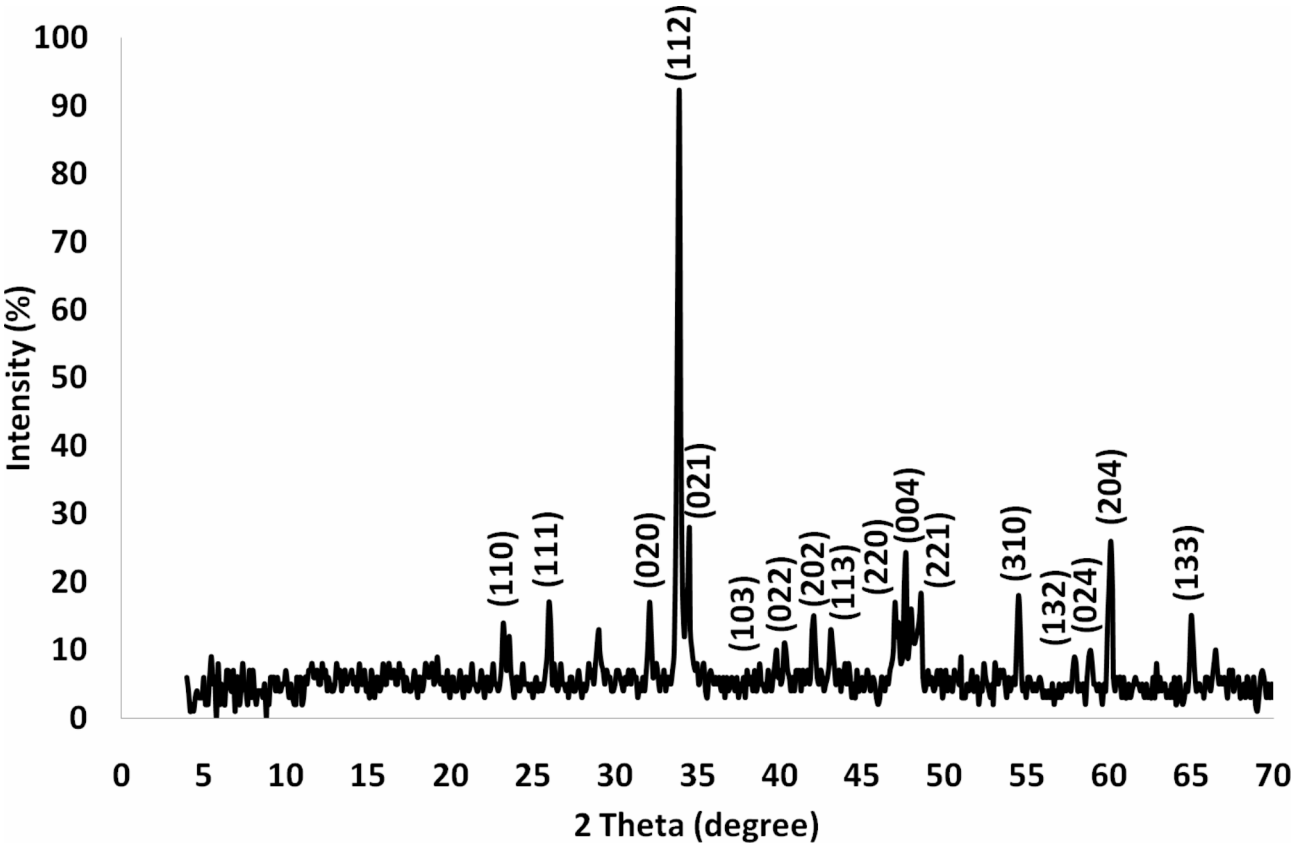

Fig. 2. XRD of filamentary Gd_2NiMnO_6 DNF.

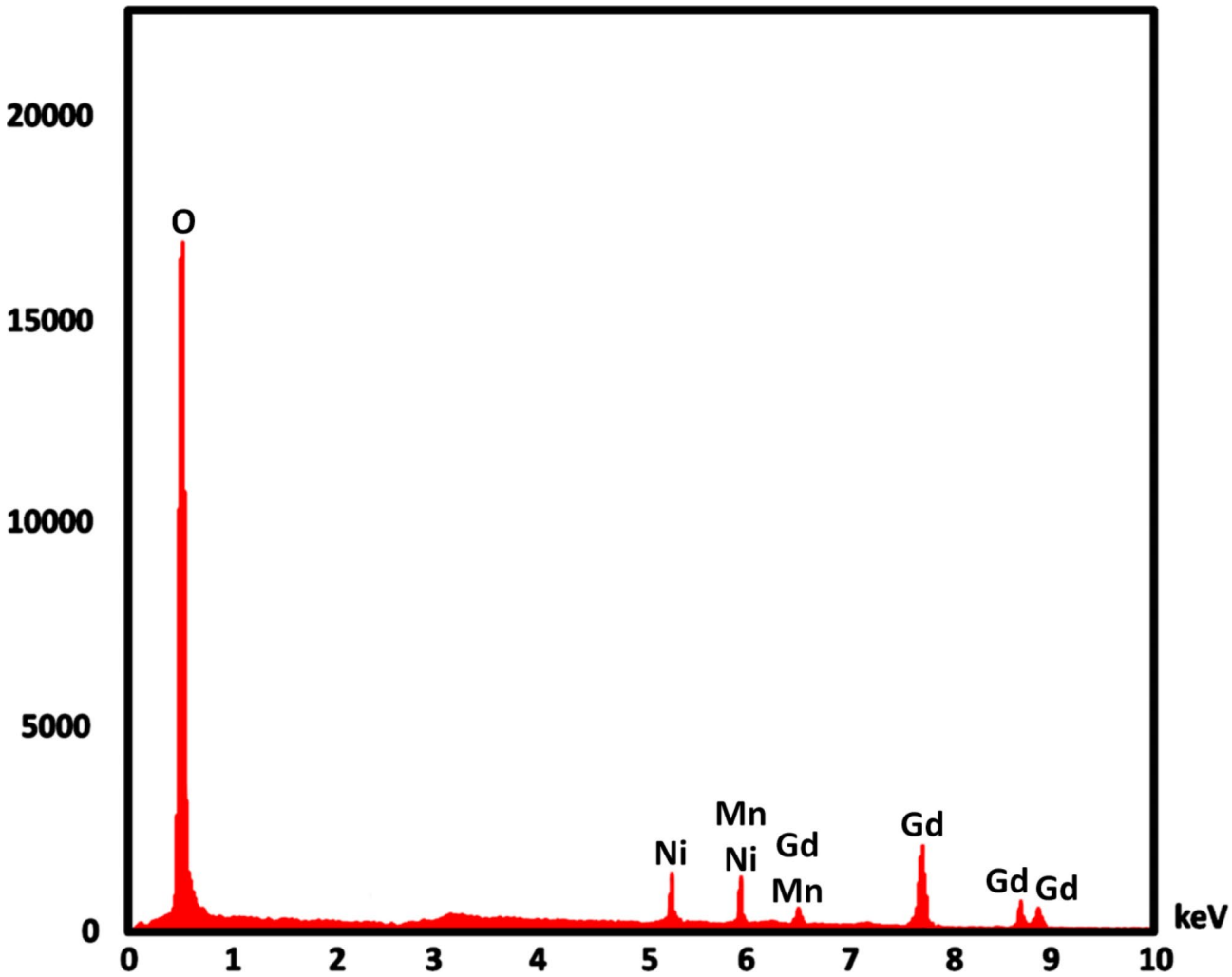

Fig. 3. EDS gamut of Gd_2NiMnO_6 DNF.

Nitrogen adsorption analysis revealed that the specific BET surface area of Gd_2NiMnO_6 DNF was approximately 674 m^2/g. The Gd_2NiMnO_6 DNF exhibited a type IV isotherm with H1-type hysteresis, indicating the existence of a mesoporous nanostructure, as shown in Fig. 5. The pore size was estimated to be around 11 nm, determined from the desorption segment of the nitrogen isotherm and calculated using the BJH method (Table 1).

To further verify the changes in the electrochemical and photochemical properties of these samples, transient photocurrent (TPC), photoluminescence (PL), and electrochemical impedance spectroscopy (EIS) were utilized to evaluate charge carrier separation efficiency (Fig. 6a-c). The Gd_2NiMnO_6 DNF exhibited reduced fluorescence intensity, increased photocurrent intensity, and a smaller radius of curvature, indicating that it performed better in photocatalysis compared to the monomer. We used DMPO to detect •OH and $•O_2^-$, and found that the Gd_2NiMnO_6 DNF did not reveal any related signals in the dark; however, the expected characteristic peaks appeared after exposure to light (Fig. 6d). In understanding the electron transfer pathway between the two photocatalysts, the work function was crucial. Electrons typically moved from the photocatalyst with a lower work function to the one with a higher work function to achieve a uniform Fermi level.

As depicted in Fig. 7a, the positive slope of the graph confirms that Gd_2NiMnO_6 exhibits n-type semiconductor properties. The flat band potential (E_{fb}) of Gd_2NiMnO_6, determined from the intercept on the potential axis, is -0.23 V versus NHE. Typically, the E_{fb} closely correlates with the conduction band minimum (E_{cb}) and for many n-type semiconductors is approximately 0.1 V lower than E_{cb}. Thus, the E_{cb} of Gd_2NiMnO_6 is estimated to be -0.89 V vs. NHE, while its valence band (E_{vb}) is calculated at around 2.41 eV vs. NHE based on its band gap. As shown in Fig. 7b, the conduction and valence band edges align with the redox potentials for CO_2 reduction and water oxidation, supporting the potential for CO_2 photoreduction in Gd_2NiMnO_6 atomic layers.

This research investigated the various factors influencing the photo-activated CO_2 reduction process, including catalyst quantity and solvent type. The findings showed that increasing the amount of Gd_2NiMnO_6 DNF positively affected CO_2 reduction, with CH_4 yield rising as catalyst loading reached up to 8 mg (Fig. 8a). Regarding the influence of the reaction medium on the photoreaction, polar solvents were found to be effective in promoting CO_2 reduction, as shown in Fig. 8b, with H_2O proving to be the most effective solvent in the study.

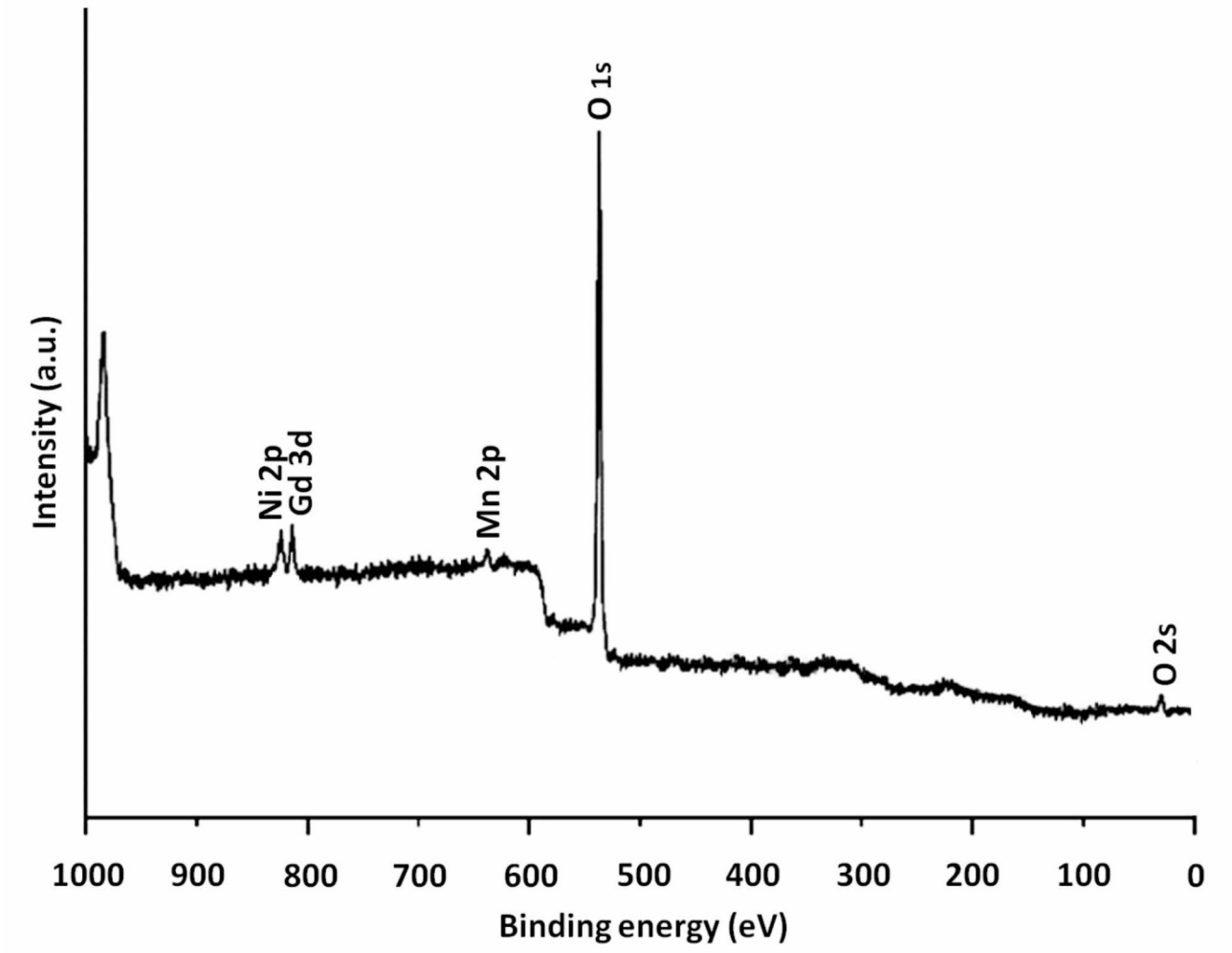

Fig. 4. XPS gamut of Gd_2NiMnO_6 DNF.

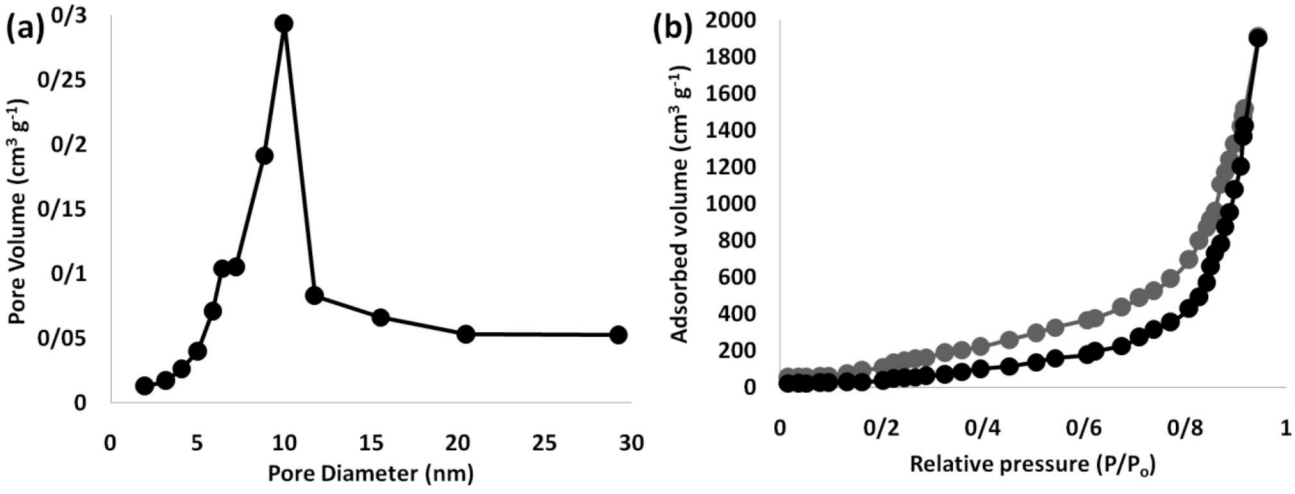

Fig. 5. The adsorption-desorption isotherms of the Gd_2NiMnO_6 DNF (**a**); and BJH pore size distributions of the Gd_2NiMnO_6 DNF (**b**).

Nanocatalysts	V_a ($cm^3\ g^{-1}$)	S_{BET} ($m^2\ g^{-1}$)	D_{BJH} (nm)
Gd_2NiMnO_6	3.4	674	11

Table 1. Structural parameters of Gd_2NiMnO_6 DNF.

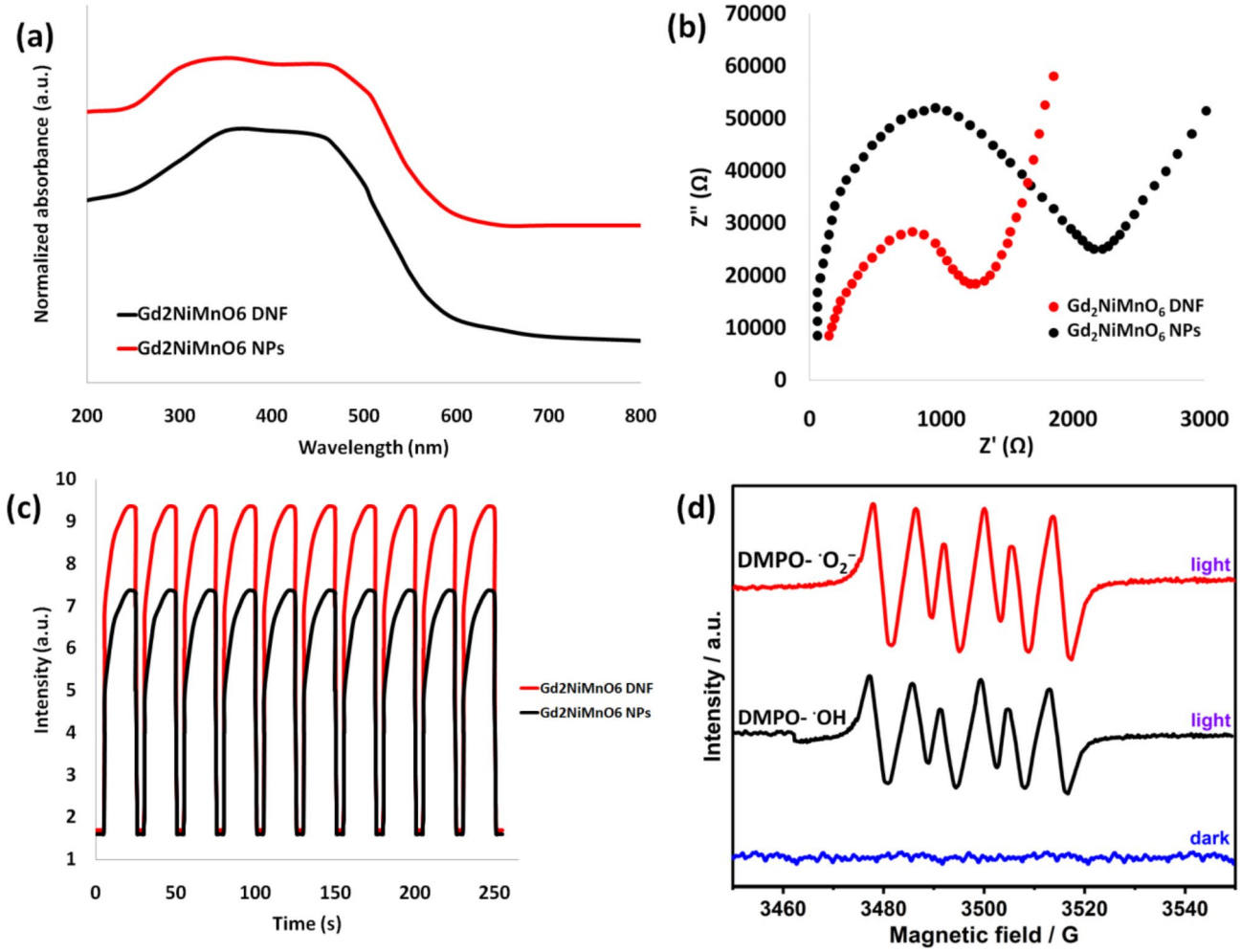

Fig. 6. (**a**) Photoluminescence spectra, (**b**) Electrochemical impedance spectroscopy, (**c**) Photocurrent spectra, and (**d**) Electron Spin Resonance spectra of Gd_2NiMnO_6 in a water-based dispersion for DMPO-·O_2^- and ·OH.

Additionally, a decline in productivity was noted when the pressure of H_2 gas was lowered. As demonstrated in Fig. 8c, the starting materials were completely converted into their respective products within 30 min.

To reduce turbidity and assess the effect of Gd_2NiMnO_6 dosage on CO_2 reduction under UV light, the mixing variable was removed by turning off the magnetic mixer during the introduction of nano-catalysts into the UV setup. The results indicated that the increase in the percentage of reduction with higher Gd_2NiMnO_6 DNF dosage was minimal compared to the results obtained with the mixing factor in the UV system. This observation was attributed to the fact that the nanocatalyst approach achieved a maximum CO_2 reduction of 98%, as indicated by the yield measurements. The difference in efficiency was evident in the absence of mixing, as illustrated in Fig. 9.

Computational analyses of the CO_2 conversion mechanism to Gd_2NiMnO_6 DNF reveal that the most thermodynamically favorable pathway involves breaking the second C – O bond at a later stage in the process, as depicted in Scheme 1. Initially, CO is formed, followed by successive hydrogenation steps producing HCO, H_2CO, and H_3CO. The resulting methoxy intermediate is subsequently reduced to form CH_4 and O. Finally, the O atom is reduced to H_2O, completing the reaction sequence.

In engineering applications, catalysts must demonstrate stability and reproducibility. As illustrated in Fig. 10, the Gd_2NiMnO_6 DNF catalysts exhibited outstanding and consistent performance in CO_2 reduction after synthesis. Notably, even after 10 cycles, the Gd_2NiMnO_6 DNF catalysts maintained a yield exceeding 95%. Our research aimed to preserve the catalyst structure during CO_2 reduction. Following the 10th cycle, we investigated this by employing various methods, as shown in Fig. 11. The XRD patterns of the regenerated catalyst (Fig. 11a)

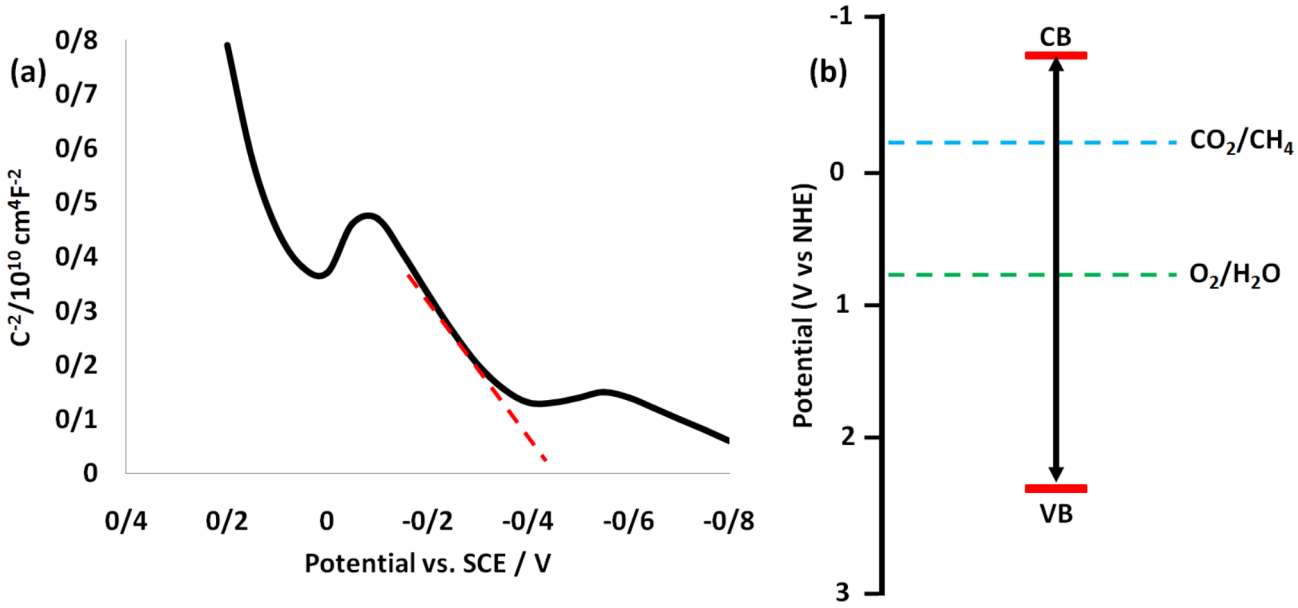

Fig. 7. (**a**) Mott-Schottky plot, and (**b**) band structure of Gd_2NiMnO_6 DNF atomic layers.

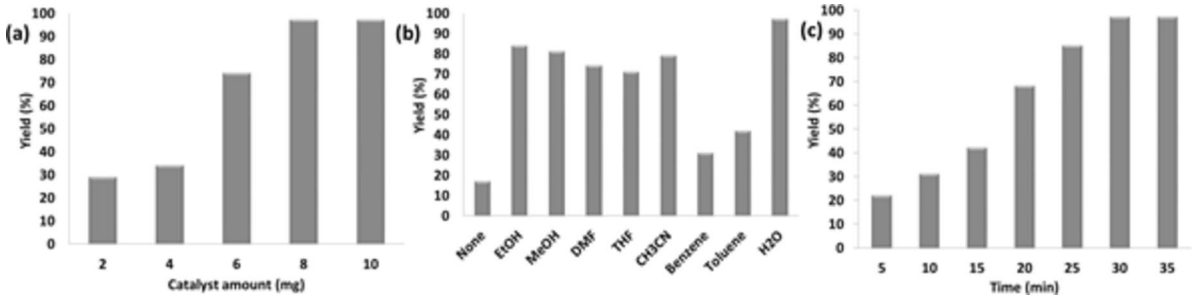

Fig. 8. Various Influences on CO_2 Reduction: (**a**) Quantity of Catalyst, (**b**) Different Solvents, and (**c**) Duration.

confirmed that the catalyst structure was entirely retained throughout the reprocessing procedure. Additionally, the TEM images of the recovered catalyst (Fig. 11b) revealed no significant changes in the nanocatalyst's morphology. The catalytic performance of Gd_2NiMnO_6 DNF was evaluated against other reported catalysts for photocatalytic CO_2 reduction (Table 2). The results demonstrated that Gd_2NiMnO_6 DNF exhibited superior product yield, affirming its higher activity compared to other catalysts.

Conclusions

We have created a series of fibers composed of Gd_2NiMnO_6 DNF that exhibit a distinct filamentous structure. These nanofibers feature impressive attributes, including numerous reactive sites, a large external surface area, and exceptional resistance to thermal and mechanical stress. The extensive external surface area, facilitated by the incorporation of interconnected channels and dendrimer-like plate nanocatalysts, makes Gd_2NiMnO_6 nanofibers a valuable choice for various scientific applications. As a result, they can be utilized in a wide array of reactions due to their outstanding properties. Furthermore, we have successfully designed a nanocatalyst that allows for precise customization of CO_2 photoreduction functionality. This enhancement was evident in the areas of H_2 evolution and CO_2 photoreduction, particularly in the selectivity for converting CO_2 into methane. Notably, the developed catalyst maintained over 94% of its activity after 10 independent cycles, demonstrating its reliable performance and reusability.

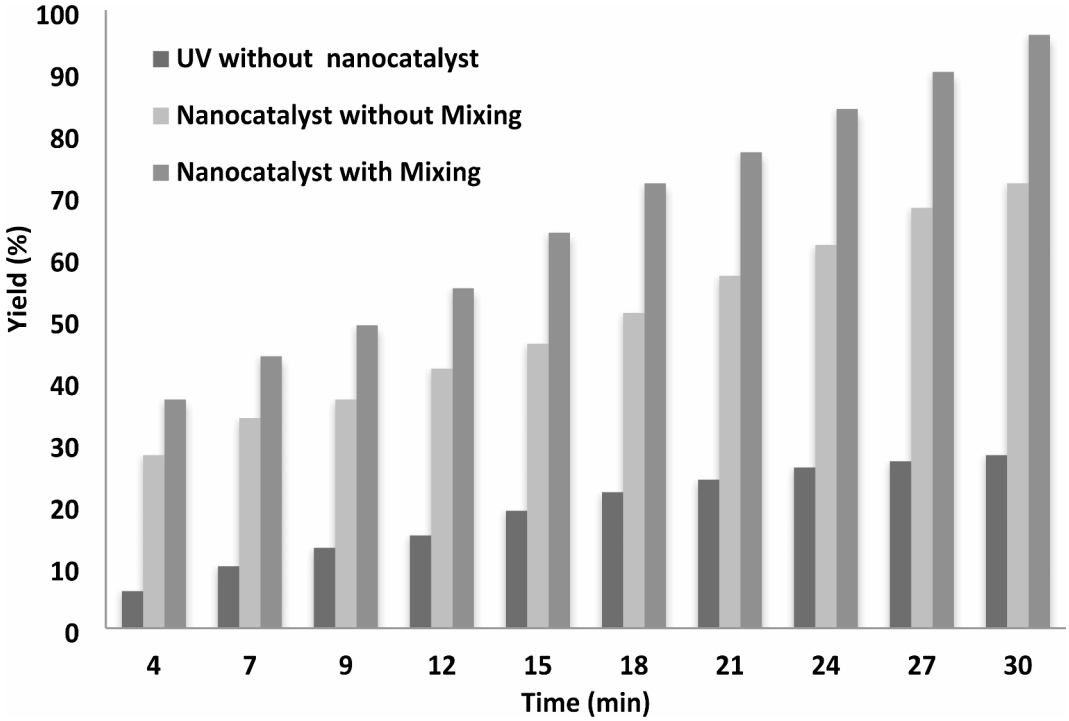

Fig. 9. Comparison of CO_2 reduction processes under optimal conditions.

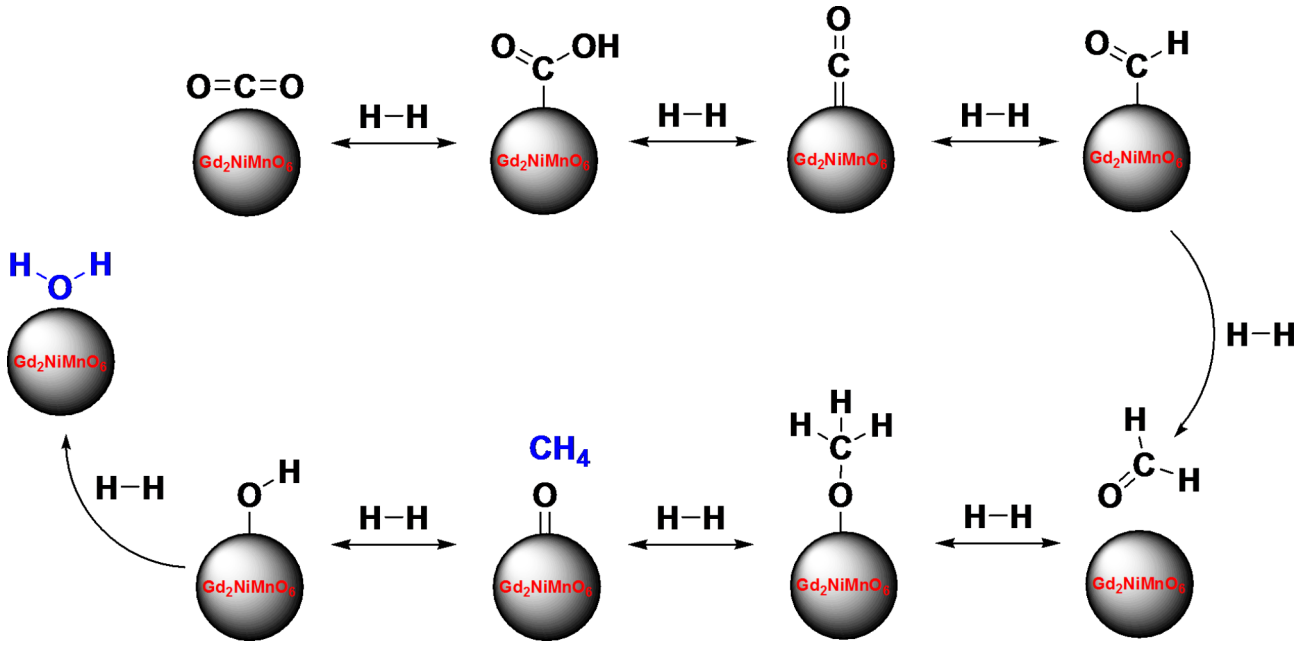

Scheme 1. Depicts the proposed catalytic pathway of Gd_2NiMnO_6 DNF, detailing the stepwise conversion of CO_2 into CH_4 through successive hydrogenation and reduction reactions.

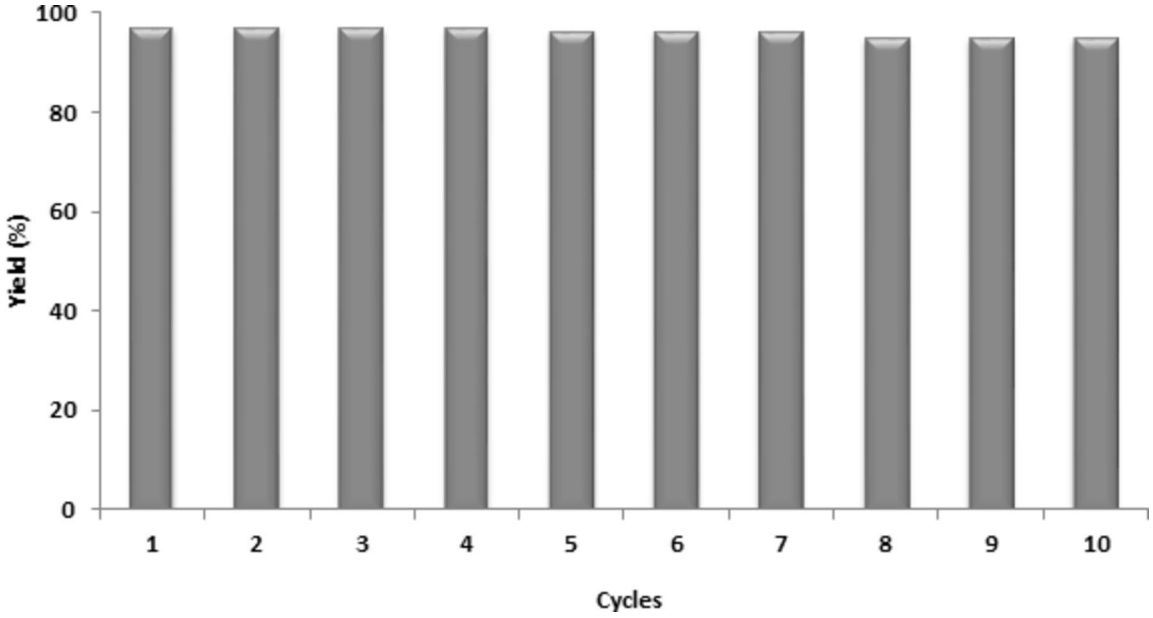

Fig. 10. Multiple experiments of Gd_2NiMnO_6 DNF in CO_2 reduction.

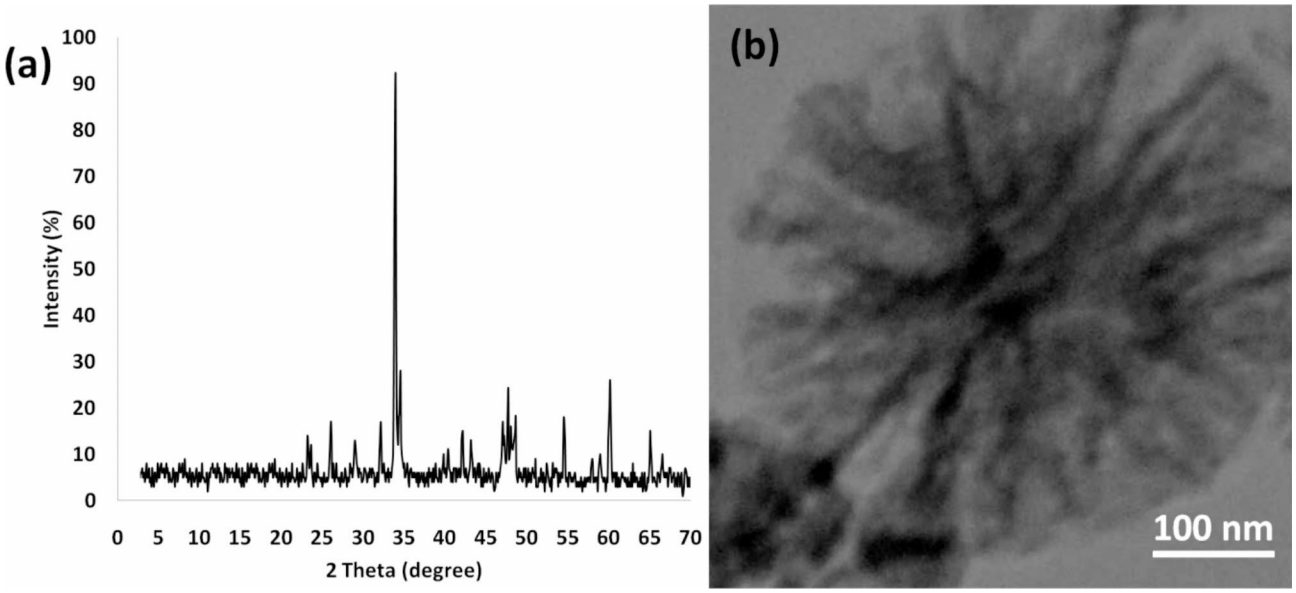

Fig. 11. (**a**) X-Ray diffraction analysis, and (**b**) transmission electron microscopy of the recycled Gd_2NiMnO_6 DNF post the 10th cycle of CO_2 reduction.

Catalyst	Solvent	Light Source	Time (h)	Product yield	Ref
$Cu_3(BTC)_2@TiO_2$	Water	UV irradiation	4	10.56 μmolg^{-1}	37
$Cu_2O@Cu@UiO-66-NH_2$	glass fiber film	300 W Xe lamp (λ > 400 nm)	5	41.5 μmolg^{-1}	38
V_S-$CuInS_8$	Water	Visible light	24	208.8 μmolg^{-1}	39
$(Au/Cu)/TiO_2$	Water	Simulated solar light	46	1400 μmolg^{-1}	40
Bi_2WO_6	Water	UV-Vis lamp		29.7 μmolg^{-1}	41
N, O, P containing polymer	Water	300 W Xe lamp (λ > 420 nm)	12	278 μmolg^{-1}	42
$CdS–WO_3$	Water	300 W Xe lamp (λ > 420 nm)		1.02 μmolg^{-1}	43
MOF-525-Co	MeCN	300 W Xe lamp (400 nm < λ < 800 nm)	6	210 μmolg^{-1}	44
MIL-101(Cr) – Ag	Glass fiber film	300 W Xe lamp (400 nm < λ < 780 nm)	18	427.5 μmolg^{-1}	45
Gd_2NiMnO_6 DNF	Water	UV irradiation	0.5	24.7 mmolg^{-1}	This Work

Table 2. Comparison of the catalytic efficiency of Gd_2NiMnO_6 DNF with various catalysts.

Data availability

All data generated or analysed during this study are included in this published article.

Received: 8 November 2024; Accepted: 8 January 2025
Published online: 13 January 2025

References

1. Xu, H. et al. Visible-Light Photoreduction of CO_2 in a Metal–Organic Framework: Boosting Electron–Hole Separation via Electron Trap States. *J. Am. Chem. Soc.* **137**,13440–13443 (2015).
2. Wang, S., Yao, W., Lin, J., Ding, Z. & Wang, X. Cobalt Imidazolate Metal–Organic Frameworks Photosplit CO_2 under Mild Reaction Conditions. *Angew Chem. Int. Ed.* **53**, 1034–1038 (2014).
3. Zhang, H. et al. Surface-Plasmon-Enhanced Photodriven CO_2 Reduction Catalyzed by Metal–Organic-Framework-Derived Iron Nanoparticles Encapsulated by Ultrathin Carbon Layers. *Adv. Mater.* **28**, 3703–3710 (2016).
4. Duan, L., Wang, L., Li, F. & Sun, L. Highly efficient bioinspired molecular Ru water oxidation catalysts with negatively charged backbone ligands. *Acc. Chem. Res.* **48**, 2084–2096 (2015).
5. Yamamoto, M. et al. Visible light-driven water oxidation using a covalently-linked molecular catalyst–sensitizer dyad assembled on a TiO_2 electrode. *Chem. Sci.* **7**, 1430–1439 (2016).
6. Wu, J. et al. Improved visible-light photocatalysis of nano-$Bi_2Sn_2O_7$ with dispersed s-bands. *J. Mater. Chem.* **21**, 3872–3876 (2011).
7. Guo, H. et al. Construction of Direct Z-Scheme AgI/$Bi_2Sn_2O_7$ Nanojunction System with Enhanced Photocatalytic Activity: Accelerated Interfacial Charge Transfer Induced Efficient Cr(VI) Reduction, Tetracycline Degradation and Escherichia coli InactivationClick to copy article link. *ACS Sustain. Chem. Eng.* **6**, 8003–8018 (2018).
8. Faria, A. C., Miguel, C. V., Ferreira, A. F. P., Rodrigues, A. E. & Madeira, L. M. CO_2 capture and conversion to methane with Ni-substituted hydrotalcite dual function extrudates. *Chem. Eng. J.* **476**, 146539 (2023).
9. Guo, X. et al. Carbon dioxide methanation over nickel-based catalysts supported on various mesoporous material. *Energy Fuels.* **32**, 3681–3689 (2018).
10. Hinojosa, B. B., Nino, J. C. & Asthagiri, A. C. First-principles study of cubic Bi pyrochlores. *Phys. Rev. B*, **77**, 104–123 (2008).
11. Murugesan, S., Huda, M. N., Yan, Y., Al-Jassim, M. M. & Subramanian, V. R. Band-engineered bismuth titanate pyrochlores for visible light photocatalysis. *J. Phys. Chem. C.* **114**, 10598–10605 (2010).
12. Morimoto, T. et al. Ring-shaped Re (I) multinuclear complexes with unique photofunctional properties. *J. Am. Chem. Soc.* **135**, 13266–13269 (2013).
13. Sadr, H., Salari, A., Ashoobi, M. T. & Nazari, M. Cardiovascular disease diagnosis: a holistic approach using the integration of machine learning and deep learning models. *Eur. J. Med. Res.* **29**, 455 (2024).
14. Alkan Saberi, Z., Sadr, H. & Yamaghani, M. R. An Intelligent Diagnosis System for Predicting Coronary Heart Disease, 10th International Conference on Artificial Intelligence and Robotics, QICAR, 131–136 (2024).
15. Nazari, M., Emami, H., Rabiei, R., Hosseini, A. & Rahmatizadeh, S. Detection of Cardiovascular Diseases Using Data Mining Approaches: Application of an Ensemble-Based Model. *Cogn. Comput.* **16**, 2264–2278 (2024).
16. Thoi, V. S. & Chang, C. J. Nickel N-heterocyclic carbene–pyridine complexes that exhibit selectivity for electrocatalytic reduction of carbon dioxide over water. *Chem. Commun.* **47**, 6578–6580 (2011).
17. Bhanja, P. et al. Supported Porous Nanomaterials as Efficient Heterogeneous Catalysts for CO_2 Fixation Reactions. *Chem. Eur. J.* **24**, 7278–7297 (2018).
18. Kudo, A. & Miseki, Y. Heterogeneous photocatalyst materials for water splitting. *Chem. Soc. Rev.* **38**, 253–278 (2009).
19. Qu, Y. & Duan, X. Progress, challenge and perspective of heterogeneous photocatalysts. *Chem. Soc. Rev.* **42**, 2568–2580 (2013).
20. Eppinger, J. & Huang, K. W. Formic Acid as a Hydrogen Energy Carrier. *ACS Energy Lett.* **2**, 188–195 (2017).
21. Mandal, K., Bhattacharjee, D. & Dasgupta, S. Synthesis of nanoporous PdAg nanoalloy for hydrogen generation from formic acid at room temperature. *Int. J. Hydrogen Energy*. **40**, 4786–4793 (2015).
22. Wang, W. H., Himeda, Y., Muckerman, J. T., Manbeck, G. F. & Fujita, E. CO_2 Hydrogenation to Formate and Methanol as an Alternative to Photo- and Electrochemical CO_2 Reduction. *Chem. Rev.* **115**, 12936–12973 (2015).
23. Rios, P., Rodriguez, A. & Lopez-Serrano, J. Mechanistic Studies on the Selective Reduction of CO_2 to the Aldehyde Level by a Bis(phosphino)boryl (PBP)-Supported Nickel Complex. *ACS Catal.* **6**, 5715–5723 (2016).
24. Kuwahara, Y., Fujie, Y. & Yamashita, H. Poly(ethyleneimine)-tethered Ir Complex Catalyst Immobilized in Titanate Nanotubes for Hydrogenation of CO_2 to Formic Acid. *ChemCatChem*. **9**, 1906–1914 (2017).
25. Carmo, M. E. G. et al. From conventional inorganic semiconductors to covalent organic frameworks: advances and opportunities in heterogeneous photocatalytic CO_2 reduction. *J. Mater. Chem. A*. **11**, 13815–13843 (2023).
26. Yu, F. et al. Molecular engineering of biomimetic donor-acceptor conjugated microporous polymers with full-spectrum response and an unusual electronic shuttle for enhanced uranium(VI) photoreduction. *Chem. Eng. J.* **466**, 143285 (2023).
27. Sun, X. et al. Solar Energy Catalysis. *Angew Chem. Int. Ed.* **61**, e202204880 (2022).
28. Zhang, Z. et al. Emerging Trends in Sustainable CO_2-Management Materials. *Adv. Mater.* **34**, 2201547 (2022).
29. Sun, K., Qian, Y. & Jiang, H. L. Metal-Organic Frameworks for Photocatalytic Water Splitting and CO_2 Reduction. *Angew Chem. Int. Ed.* **62**, e202217565 (2023).

30. Xiong, X. et al. Selective photocatalytic CO_2 reduction over Zn-based layered double hydroxides containing tri or tetravalent metals. *Sci. Bull.* **65**, 987–994 (2020).
31. Xiong, X. et al. Photocatalytic CO_2 Reduction to CO over Ni Single Atoms Supported on Defect-Rich Zirconia. *Adv. Energy Mater.* **10**, 2002928 (2020).
32. Zhao, Y. et al. Defect-Rich Ultrathin ZnAl-Layered Double Hydroxide Nanosheets for Efficient Photoreduction of CO_2 to CO with Water. *Adv. Mater.* **27**, 7824–7831 (2015).
33. Jia, G. et al. Ultrathin origami accordion-like structure of vacancy-rich graphitized carbon nitride for enhancing CO_2 photoreduction. *Carbon Energy*. **5**, e270 (2023).
34. Zhang, K. et al. Sustainable CO_2 management through integrated CO_2 capture and conversion. *J. CO_2 Util.* **72**, 102493 (2023).
35. Sun, Z. et al. Research progress in metal–organic frameworks (MOFs) in CO_2 capture from post-combustion coal-fired flue gas: characteristics, preparation, modification and applications. *J. Mater. Chem. A*. **10**, 5174–5211 (2022).
36. Xu, Y. et al. Tuning ionic liquid-based functional deep eutectic solvents and other functional mixtures for CO_2 capture. *Chem. Eng. J.* **463**, 142298 (2023).
37. Li, R. et al. Integration of an inorganic semiconductor with a metal-organic framework: a platform for enhanced gaseous photocatalytic reactions. *Adv. Mater.* **26**, 4783–4788 (2014).
38. Wang, S. Q., Zhang, X. Y., Dao, X. Y., Cheng, X. M. & Sun, W. Y. Cu_2O@Cu@UiO-66-NH_2 Ternary Nanocubes for Photocatalytic CO_2 Reduction. *ACS Appl. Nano Mater.* **3**, 10437–10445 (2020).
39. Li, X. et al. Selective visible-light-driven photocatalytic CO_2 reduction to CH_4 mediated by atomically thin $CuIn_5S_8$ layers. *Nat. Energy*. **4**, 690–699 (2019).
40. Neatu, S., Maciá-Agulló, J. A., Concepción, P. & Garcia, H. Gold–Copper Nanoalloys Supported on TiO_2 as Photocatalysts for CO_2 Reduction by Water. *J. Am. Chem. Soc.* **136**, 15969–15976 (2014).
41. Lu, C. et al. Constructing Surface Plasmon Resonance on Bi_2WO_6 to Boost High-Selective CO_2 Reduction for Methane. *ACS Nano*. **15**, 3529–3539 (2021).
42. Guo, S. et al. Visible-Light-Driven Photoreduction of CO_2 to CH_4 over N,O,P-Containing Covalent Organic Polymer Submicrospheres. *ACS Catal.* **8**, 4576–4581 (2018).
43. Jin, J., Yu, J., Guo, D., Cui, C. & Ho, W. A Hierarchical Z-Scheme CdS-WO_3 Photocatalyst with Enhanced CO_2 Reduction Activity. *Small*. **11**, 5262–5271 (2015).
44. Zhang, H. et al. Efficient Visible-Light-Driven Carbon Dioxide Reduction by a Single-Atom Implanted Metal–Organic Framework. *Angew, C. Int. Ed.* **55**, 14310–14314 (2016).
45. Guo, F. et al. Size Engineering of Metal–Organic Framework MIL-101(Cr)–Ag Hybrids for Photocatalytic CO_2 Reduction. *ACS Catal.* **9**, 8464–8470 (2019).

Acknowledgements

This work was sponsored in part by The University Synergy Innovation Program of Anhui Province(GXXT-2023-028, GXXT-2022-086), Intelligent computing theory and application of excellent scientific research and innovation team of Anhui Province (2023AH010044).

Author contributions

Ping Yan: Conceptualization, Methodology, Writing - Original DraftDulong Feng: Investigation, Software, Formal analysisQian Wan: Investigation, Resources, Data CurationShulong Liu: Project administrationSeyed Mohsen Sadeghzadeh: Project administration.

Declarations

Competing interests

The authors declare no competing interests.

Additional information

Correspondence and requests for materials should be addressed to S.M.S.

Reprints and permissions information is available at www.nature.com/reprints.

Publisher's note Springer Nature remains neutral with regard to jurisdictional claims in published maps and institutional affiliations.

Open Access This article is licensed under a Creative Commons Attribution-NonCommercial-NoDerivatives 4.0 International License, which permits any non-commercial use, sharing, distribution and reproduction in any medium or format, as long as you give appropriate credit to the original author(s) and the source, provide a link to the Creative Commons licence, and indicate if you modified the licensed material. You do not have permission under this licence to share adapted material derived from this article or parts of it. The images or other third party material in this article are included in the article's Creative Commons licence, unless indicated otherwise in a credit line to the material. If material is not included in the article's Creative Commons licence and your intended use is not permitted by statutory regulation or exceeds the permitted use, you will need to obtain permission directly from the copyright holder. To view a copy of this licence, visit http://creativecommons.org/licenses/by-nc-nd/4.0/.

© The Author(s) 2025